Polymer 228 (2021) 123850

Contents lists available at ScienceDirect

Polymer

journal homepage: www.elsevier.com/locate/polymer

Prediction of morphology development within micro–injection molding samples

Vito Speranza [a], Sara Liparoti [a,*], Roberto Pantani [a], Giuseppe Titomanlio [a,b]

[a] Department of Industrial Engineering, University of Salerno – via Giovanni Paolo II, 132, 84084, Fisciano (SA), Italy
[b] Institute of Polymers, Composites and Biomaterials (IPCB), The National Research Council – via Previati 1/C, 23900, Lecco (LC), Italy

ARTICLE INFO

Keywords:
Flow induced crystallization
Micro–injection molding
Shish kebab
Morphology prediction

ABSTRACT

The understanding of the mechanisms that determines mechanical performances during micro-injection molding is crucial to meet the increasing demand for advanced plastic products with improved durability and performance. These depend on the morphology developed during the process, which, on its turn, is determined by the complex thermomechanical history experienced by polymer chains. Thus, the ability to correctly predict morphology opens the possibility to forecast final part properties. Semi-crystalline polymers parts show a morphology mainly composed of spherulites in the core and fibrils close to the sample walls. In this work, a commercial software for injection molding simulation was adopted for describing the thermomechanical history experienced by polymer chains during micro–injection molding tests, whereas a crystallization model was introduced for the description of the two morphologies mentioned above. The molecular stretch parameter was adopted as the main variable for describing the effect of flow on the molecular arrangement. A threshold mechanism based on the molecular stretch was also introduced in the crystallization model for controlling the growth of fibrillar morphologies. Different micro-injection molding tests were conducted in an end-less cavity with the aim of testing the capability of the model in predicting the morphology developed along the sample thickness. The proposed model was able to predict the formation of fibrils in the regions close to the sample wall, furthermore, the reduction of fibrillar layer thickness with the mold temperature increase was consistently described.

1. Introduction

The increasing request for advanced plastic products coupled with the necessity of increasing mechanical performances and durability of plastic parts are promoting high performance polymer processes [1,2]. Micro-injection molding is certainly a core technology for the production of high-value-added plastic parts [3]. It mainly consists of three stages: polymer melting, injection of the melt into a mold cavity, part cooling down to the extraction temperature.

The molded object properties strongly depend on the distribution of morphologies and crystalline structures developed during the process [4,5]. Molded samples generally show skin-core morphology, with a poorly oriented skin, a highly oriented shear layer (composed of fibrils in the case of many semicrystalline polyolefins) and a more isotropic core (composed of spherulites) [3,6]. Morphology determines the mechanical performances of the molded objects. Jiang et al. [7,8] measured modulus distribution within injection molded parts by nanoindentation. They found that the shear layers are characterized by higher modulus than both the core and the skin layers. They attributed the distribution of the mechanical properties to the crystalline phase distribution: the presence of β-crystals in the moldings obtained with low shear rates and high temperatures induced a toughening increase. Wang et al. [9] demonstrated that an alternation of the crystalline structures and morphologies within the semicrystalline moldings leads to a change in the creep behavior. Zhou et al. [10] induced the increase of the shear layer thickness by pressure vibration injection molding. They found that the tensile strength improved significantly with the increase of the shear layer thickness. Kuzmanović et al. [11] found that there is a strong relationship among processing temperature, morphology and mechanical properties. The aforementioned works highlighted the necessity of understanding the relationship between the process and the formation of hierarchical structures, which, on their turn, determine the other properties of the molding parts. To this purpose many authors proposed models for describing the injection molding process, accounting for the

* Corresponding author.
E-mail addresses: vsperanza@unisa.it (V. Speranza), sliparoti@unisa.it (S. Liparoti), rpantani@unisa.it (R. Pantani), gtitomanlio@unisa.it (G. Titomanlio).

https://doi.org/10.1016/j.polymer.2021.123850
Received 1 March 2021; Received in revised form 30 April 2021; Accepted 4 May 2021
Available online 16 May 2021
0032-3861/

phenomena which lead to the formation of the final morphology.

Zhao et al. [12] introduced a method for the prediction of the average crystallinity during injection molding. The predicted overall crystallinity degree was found consistent with the experimental results obtained from calorimetric analyses conducted on the moldings. However, this model was not able to describe the morphologies developed during the process. Laschet et al. [13] developed a multi-scale simulation, coupling macroscale mold filling, and the heat transfer analysis, with a microscale crystallization model. The spherulite growth description allowed the prediction of spherulite diameter that was found consistent with the experimental observations. The aforementioned model only accounted for the formation of the spherulites; they did not describe the fibrils formation into the shear layer. In order to describe the formation of fibrils, some authors introduced models for taking into account the effect of flow on crystallization. A modified Nakamura model was proposed for describing the enhancement of crystallization kinetics via the melting temperature increase due to the flow [14]. This modeling approach was based on the chain extension analysis: the chain extension induces a decrease in polymeric melt entropy, thus, an increase in both crystalline temperature and crystallization kinetics. Koscher and Fulchiron [15] found that flow promotes a nucleation enhancement. In most cases, the analysis of crystallization was conducted under controlled shear rate and isothermal conditions. Graham and coworkers analyzed the effect of polydispersity on the promotion of crystallization into oriented structures and hypothesized that the critical nuclei were enriched of longer chains, giving a super-exponential dependence of the nucleation rate on shear [16]. Ryan and coworkers [17,18], following Janeschitz-Kriegl's hypothesis [19] that the work done on a sheared polymer melt controls the resulting morphology, also confirmed by Van Puyvelde et at [20], found that the critical work required for orientation decreases with an increasing fraction of high molecular weight molecules. Pantani et al. [21], starting from the considerations of Van Puyvelde and Ryan, introduced a model for predicting the fibrils formation during injection molding. This model was based on the achievement of both a critical molecular stretch and a critical mechanical work to guarantee sufficient time for molecular structuring into fibrils. Such a criterion was able to predict the formation of hierarchical structures when fast modulation of mold temperature was adopted [22]. Wang et al. [23] adopted a phase field approach, for tracing the spherulite interface, coupled with a model for the prediction of stretch experienced by polymer chains during the process. The crystallization process was divided into two stages: flow induced nucleation, and subsequent crystal growth after flow cessation. The model was able to predict where fibrils replaced spherulites along the sample thickness.

All the aforementioned models adopted the spherulite crystallization kinetics for predicting also the formation of the fibrils, even if the fibril growth is considered to occur mostly along the flow direction, vice-versa the spherulitic growth is considered isotropic. Peters et al. [24,25] introduced a model for the crystallization into fibrils. Speranza et al. [26] proposed a model for prediction of fibril formation during isothermal experiments conducted with Linkam shearing cell. Via comparison with experimental data, such a model demonstrated to be more efficient in predicting the fibril formation than the other proposed models. In this work, the model for the crystallization into fibrils in the presence of flow was introduced for predicting the morphology development by effect of flow and it was applied to the micro-injection molding process. Commercial software was adopted for the prediction of the temperature and flow fields during different stages of the process. The simulation outcomes were adopted as input for the introduced model to describe crystallization into spherulites and fibrils. The findings of the overall model, in terms of morphology developed along the sample thickness, were compared with the experimental results. To this purpose, different injection molding experiments were conducted with different mold temperatures, which were found to be the main parameter affecting the morphology during the process [27,28].

2. Materials and methods

The injection molding tests were conducted adopting an HAAKE Minijet II micro–injection molding machine by Thermo Scientific (Waltham, MA, USA). It is a piston injection molding machine which adopts a vertical injection system. An isotactic polypropylene, iPP (T30G, Basell, Ferrara, Italy), was adopted for injection molding tests. It was previously characterized with respect to rheology and crystallization kinetics (under both quiescent and flow conditions) [29]. Cavity geometry and dimensions are shown in Fig. 1. The cavity had a thickness of 0.5 mm. For all tests, a melt temperature of 220 °C and an injection pressure of 400 bar were adopted. Injection pressure was released after 1 s. Three different molding conditions, indicated in the following as condition A, B and C, were considered with different mold temperatures 40 °C, 110 °C and 140 °C respectively.

The cooling of the mold started after 7 s by using water at 25 °C. For each condition, five tests were performed.

Simulations of the injection molding tests were conducted by Moldex3D version R17 from CoreTech System Ltd (Chupei City, Taiwan). A material database was generated, describing the material properties accordingly to the characterizations reported in previous works. In particular, material viscosity and pressure-volume-temperature behavior were described adopting a Cross-WLF model and a modified Tait equation, respectively [29,30]. A single freeze temperature of 150 °C was adopted for the simulations. A mesh with 113262 tetrahedral elements and 132724 nodes was generated for the simulations.

Thin slices (100 μm thick) were cut from each sample at 6 mm downstream from the cavity inlet point, in the flow-thickness plane by Leica RM 2265 slit microtome (Wetzlar, Germany). The slices were observed by Olimpus BX51 (Segrate, Milano, Italy) optical microscope with crossed polarizers. The flow direction was rotated of 45° with respect to the direction of one of the polarizers.

3. Crystallization model

In order to describe the morphology distributions developed during the injection molding test within the molded samples, a model for the crystallinity evolution has to be adopted. The iPP adopted for the molding tests was deeply characterized with respect to the crystallization toward the different morphologies of the α–phase (both under flow and under quiescent conditions) and the relationships between rheology and crystallization [26] was also investigated. The α–phase was found to be the predominant phase within molded samples made of the adopted iPP grade [31]. Kolmogorooff's equation was adopted to describe the crystallinity evolution into spherulitic morphology. Such an equation can be solved by adopting Schneider's solution approach:

$$\phi_0(t) = \frac{4}{3}\pi \int_{-\infty}^{t} \dot{N}_s(s) \left[\int_{s}^{t} G_s(u)du \right]^3 ds = V_{tot}$$

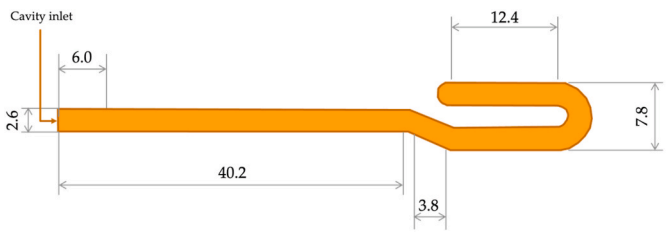

Fig. 1. Cavity geometry and dimensions, given in millimeters. The position selected for optical investigation, 6 mm downstream from the cavity inlet, is also shown.

$$\phi_1(t) = 4\pi \int_{-\infty}^{t} \dot{N}_s(s) \left[\int_{s}^{t} G_s(u)du \right]^2 ds = S_{tot}$$

$$\phi_2(t) = 8\pi \int_{-\infty}^{t} \dot{N}_s(s) \left[\int_{s}^{t} G_s(u)du \right] ds = 8\pi R_{tot}$$

$$\phi_3(t) = 8\pi \int_{-\infty}^{t} \dot{N}_s(s)ds = 8\pi N_s \tag{1}$$

where ϕ_0 represents the total volume, V_{tot}, occupied by the spherulites; ϕ_1 represents the total surface, S_{tot}, exposed by the spherulites to further crystallization; ϕ_2 represents equivalent total radius, R_{tot}, of the spherulites and ϕ_3 represents the total number, N_s, of the spherulites; $\dot{N}_s$ is the spherulitic nucleation rate and G_s is the spherulitic growth rate.

A similar approach was proposed for the description of the crystallization into fibrils (namely shish kebabs), which described the growth of structures mainly along the flow direction. These structures also grow along the lateral direction. The fibrillar crystallinity evolution is given by the following set of integral equations (2)

$$\psi_0(t) = 2\pi \int_{-\infty}^{t} \dot{N}_f(s) \int_{s}^{t} G_f(u) \left[\int_{u}^{t} G_{lat}(p)dp \right]^2 duds = V_{tot}$$

$$\psi_1(t) = 4\pi \int_{-\infty}^{t} \dot{N}_f(s) \int_{s}^{t} G_f(u) \int_{u}^{t} G_{lat}(p)dp\, duds = S_{tot}$$

$$\psi_2(t) = 4\pi \int_{-\infty}^{t} \dot{N}_f(s) \int_{s}^{t} G_f(u)duds = 4\pi L_{tot}$$

$$\psi_3(t) = 4\pi \int_{-\infty}^{t} \dot{N}_f(s)ds = 4\pi N_f \tag{2}$$

where N_f is the number of fibrils (with nucleation rate $\dot{N}_f$), G_f is the fibril axial growth rate and G_{lat} is the fibril lateral growth rate, V_{tot} is the total volume of fibrils, S_{tot} is the fibril total surface, and L_{tot} is the fibril total length. Fibrillar and spherulitic morphologies compete for the same available amorphous volume. The total relative crystallinity, ξ, is obtained by the Kolmogoroff–Avrami's equation (3):

$$-\ln(1-\xi) = \phi_0 + \psi_0 \tag{3}$$

The proposed model (equations (1)–(3)) is able to describe the morphology evolutions once the growth and nucleation rates are defined. In order to achieve a realistic prediction of the morphology, the effect of flow on the structure formation has to be considered [32]. To this purpose the non-linear Maxwell's model was adopted to describe the rate of change of the molecular conformational tensor $\boldsymbol{A}$

$$\frac{D\boldsymbol{A}}{Dt} - (\nabla \boldsymbol{v})^T \cdot \boldsymbol{A} - \boldsymbol{A} \cdot (\nabla \boldsymbol{v}) = -\frac{1}{\lambda(\boldsymbol{A})}\boldsymbol{A} + (\nabla \boldsymbol{v})^T + (\nabla \boldsymbol{v}) \tag{4}$$

The detailed procedure followed to obtain equation (4) is reported in Appendix A.

Such a model describes the molecular stretch evolution during the process, once the velocity gradient, $\nabla \boldsymbol{v}$, and the relaxation time λ are known. In simple shear flow (for detailed description see Appendix A), the aforementioned equation becomes (5):

$$\frac{\partial A_{11}}{\partial t} - 2\dot{\gamma}A_{12} + \frac{A_{11}}{\lambda} = 0$$

$$\frac{\partial A_{12}}{\partial t} + \frac{A_{12}}{\lambda} - \dot{\gamma} = 0 \tag{5}$$

where the subscript "1" identifies the flow direction, and the subscript "2" identifies the transverse (sample thickness) direction. $\dot{\gamma}$ is the shear rate, given by equation (6):

$$\dot{\boldsymbol{\gamma}} = (\nabla \boldsymbol{v}) + (\nabla \boldsymbol{v})^T \tag{6}$$

where $\dot{\gamma} = \sqrt{\frac{1}{2}\dot{\boldsymbol{\gamma}} : \dot{\boldsymbol{\gamma}}}$.

The relaxation time λ depends on the stretch parameter Δ [32,33], according to equation (7):

$$\lambda(T,\ P, \chi, \Delta) = \frac{\lambda_0 \cdot \alpha(T,\ P, \chi)}{1 + (a\Delta)^b} \tag{7}$$

a and b are material parameters, λ_0 is the relaxation time at rest, and Δ is a measure of the molecular stretch, namely the largest difference between the eigenvalues of the molecular conformation tensor $\boldsymbol{A}$. In simple shear flow Δ is expressed as (8):

$$\Delta = \sqrt{A_{11}^2 + 4A_{12}^2} \tag{8}$$

The dependence of the relaxation time λ upon temperature, pressure and total crystallinity, χ, is given by α ((9) [34]).

$$\alpha(T, P, \chi) = 10^{\frac{-c_1(T-T_0-C_3P)}{C_2+T-T_0}} \cdot \delta(\chi) \tag{9}$$

where δ is given by (10)

$$\delta(\chi) = e^{h\chi^2} \tag{10}$$

where h is a material parameter. Experiments conducted by Linkam shearing cell under isothermal conditions on T30G revealed that both nucleation density and growth rate change because of the flow application, for spherulitic morphology [35]. This effect was accounted for by the increase of the melting temperature with the stretch, as mentioned in the introduction. The Hoffman–Lauritzen's equation for the description of spherulitic growth rate has to account for the effect of stretch on the melting temperature, T_m.

$$G_s = G_0 \exp\left(-\frac{U}{R(T - T_\infty)} \right) \exp\left(-\frac{K_g(T + T_m(\Delta))}{2T^2(T_m(\Delta) - T)} \right) \tag{11}$$

T_m in equation (11) is considered dependent upon molecular stretch, Δ, according to the phenomenological equation (12):

$$T_m(\Delta) = \max\left(T_{m,0}; M_1 \left[\tanh\left(\frac{\Delta - M_2}{M_3} \right) - 1 \right] + \frac{M_4}{1 + M_5 e^{-M_6 \Delta}} \right) \tag{12}$$

A recent work on the formation of fibrils under controlled shear rates in isothermal conditions revealed that both the fibril growth rates [26] G_f and G_{lat}, can be considered dependent on the flow, through the molecular stretch parameter Δ, according to the following equations

$$\begin{aligned} G_f(\Delta) &= A_0 \cdot \Delta^b \\ G_{lat}(T,\ \Delta) &= G_s(T,\ \Delta) \end{aligned} \tag{13}$$

For spherulitic crystallization under flow conditions, the nucleation rate is related to the excess of growth rate due to the flow with respect to its quiescent value (namely, G_q)

$$\dot{N}_s = \max\left[B_1 \left(G_s(\Delta) - G_q \right)^{\ell}; B_2 \left(G_s(\Delta) - G_q \right)^{h} \right] \tag{14}$$

The effect of flow on the nucleation density can be described as follows (15):

$$N_s = \frac{N_0}{\left(1 + A_n \exp\left(B_n \left(T - T_{m,0}\right)\right)\right)} + \int_{-\infty}^{t} \dot{N}_s(s)ds \tag{15}$$

where the first term accounts for the predetermined nuclei which depend on temperature, only (heterogeneous nucleation).

The fibril nucleation rate (16) depends on the excess of axial growth rate with respect to the quiescent spherulitic growth rate, G_q. A correlation similar to the one considered for the spherulitic crystallization (equation (14)) was adopted:

$$\dot{N}_f = \max\left[B_1\left(G_f(\Delta) - G_q\right)^{\ell}; B_2\left(G_f(\Delta) - G_q\right)^{\hbar}\right] \quad (16)$$

The parameters adopted for the equations from (1) to (16) are given in Table 1. The model for crystallization was validated by Linkam shearing tests conducted under controlled shear rates and isothermal conditions [26]. The formation of fibrillar structures was followed at the observation window during those tests carried out at temperature of 140 °C. In particular, for each shear rate applied during the single test, the time required for the formation of fibrillar structures was identified. Moreover, when shear rates lower than 0.7 s^{-1} were adopted, the formation of fibrils was not observed, even for very long shearing times (of the order of several minutes). The molecular stretch parameter, Δ, was chosen as the characteristic variable of the effect of flow on the molecular arrangement. The calculation of the molecular stretch values for the conditions adopted during Linkam shearing tests allowed the identification of a threshold value for the molecular stretch (Δ_{min}= 2.5) below which fibrils do not form. The identification of that threshold value is a step forward with respect to the model proposed in Ref. [26], which predicted the formation of fibrils whatever molecular stretch. The detailed description of the method followed for the identification of the threshold and the evaluation of the fibrillar axial growth, G_f, is reported in Appendix B.

In the following, the model developed above is applied, for the first time, to real processing conditions, where temperature and velocity gradients are not constant both along the flow direction and over time.

4. Results

The final filling length of the molded objects depends on the adopted mold temperature: the lower is the mold temperature, the smaller is the final filling length. Injection molding experiments conducted with different mold temperatures were adopted to validate the outcomes of the simulations by Moldex3D. The cavity adopted for the experimental tests can be considered an endless cavity: since with the adopted mold temperature the solidification occurs before the polymer can completely fill the cavity [36]. Fig. 2 shows the comparison between the final filling length experimentally found and the final filling length evaluated by Moldex3D simulations.

The final filling length increases with mold temperature due to a slower solidification of the material when high mold temperatures are adopted. The final filling lengths evaluated by Moldex3D simulations are consistent with those experimentally observed, except at the lowest mold temperature. This discrepancy can be ascribed to the fact that the material behavior is influenced by crystallinity evolution. In particular, the material solidification is determined by the crystallization and the molecular stretch-crystallization interplay. These effects, which are not accounted for in Moldex3D, become more significant as the mold temperatures decrease.

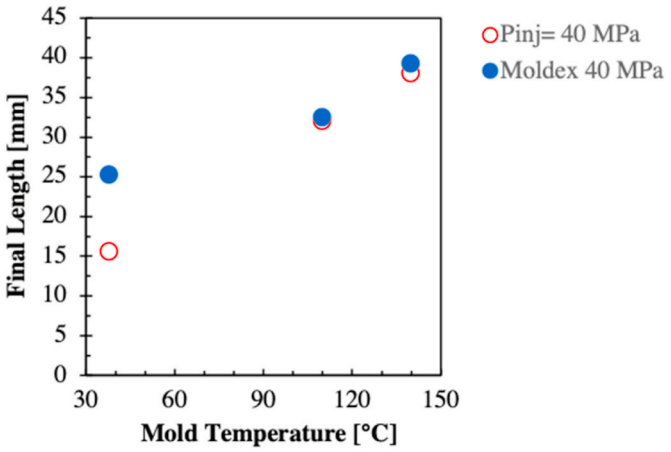

Fig. 2. The final filling length obtained from the molding tests and from Moldex3D simulations.

The aforementioned crystallization model is coupled in the following with the temperature and shear rate evolutions, obtained using Moldex3D, to predict morphology. Firstly, the morphology developed during the process in samples obtained with different mold temperatures was analyzed by optical microscopy. Fig. 3 shows the optical micrographs, obtained with crossed polarizers, of the half thickness of the moldings produced with 40 °C, 110 °C, and 140 °C mold temperatures. Beside each micrograph, a graded colored bar helps to identify layers characterized by different morphologies. All micrographs were taken at 6 mm downstream of the cavity entrance (see Fig. 1 for the cavity sketch).

The micrographs in Fig. 3 allow to identify at least two different morphologies along the sample thickness: colored bands are always present close to the sample surface whereas granular structures characterize the sample core. The colored bands are composed of fibrils, whereas the granular core is composed of spherulites. A detailed description of the method adopted for the identification of the layers on the optical micrographs is reported elsewhere [28,37]. The oriented structures (namely the colored bands) cover the whole sample thickness in the molding obtained with 40 °C mold temperature. The spherulitic core (namely granular structures) is detectable when mold temperatures of 110 °C or 140 °C are adopted. Furthermore, in the molded samples obtained with 110 °C mold temperature a transition zone, characterized by structures with intermediate morphology between spherulites and fibrils, is clearly visible. The thickness of such a transition zone reduces as the mold temperature increases. The thickness of the oriented layer depends upon the mold temperature: in particular, such a thickness decreases as the mold temperature increases. Consistently, the sample core enlarges when mold temperature increases.

Starting from the temperature and shear rate evolutions calculated with Moldex3D, the developed procedure allows to calculate the molecular stretch evolution for several distances from the sample midplane. Fig. 4a and b shows shear rate, temperature and molecular stretch, Δ, evolutions calculated for condition A (mold temperature 40 °C) at two different distances from the sample midplane, 15 μm and 170 μm, in the same axial position where the optical micrographs of Fig. 3 were taken.

Fig. 4a shows that the temperature along the sample thickness

Table 1
Parameters adopted in the model described by equations from (1) to (16).

Parameter	Value	Equation	Parameter	Value	Equation
λ_0 [s]	14	7	M_2 [−]	1.1	12
a [−]	3.8	7	M_3 [−]	0.2	12
b [−]	2.2	7	M_4 [K]	490.11	12
C_1 [−]	2.5	9	M_5 [−]	0.041	12
C_2 [K]	301.4	9	M_6 [−]	0.09	12
C_3 [K/bar]	0.18	9	A_0 [μm/s]	0.0004	13
T_0 [K]	503.00	9	b [−]	5	13
h [−]	180	10	B_1 [$1/(\mu m^{3+\ell}\, s^{1+\ell})$]	$2\ 10^{-9}$	14, 16
G_0 [cm/s]	1380	11	ℓ [−]	0.5	14, 16
U/R [K]	751.6	11	B_2 [$1/(\mu m^{3+\hbar}\, s^{1+\hbar})$]	$3\ 10^{-6}$	14, 16
T_∞ [K]	198.46	11	$\hbar$ [−]	2	14, 16
K_g [K^2]	371381	11	N_0 [nuclei/cm^3]	$1.95\ 10^9$	15
$T_{m,0}$ [K]	467.54	12	A_n [−]	$1.3\ 10^8$	15
M_1 [K]	4	12	B_n [K^{-1}]	0.155	15

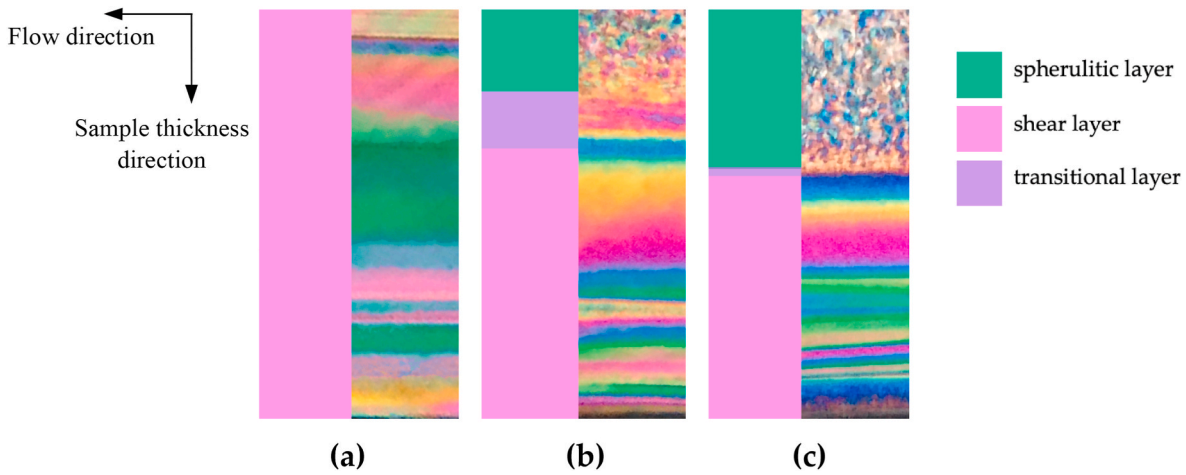

Fig. 3. Optical micrographs of the half thickness of the molded samples obtained with different mold temperatures: (a) A – 40 °C; (b) B – 110 °C; (c) C – 140 °C.

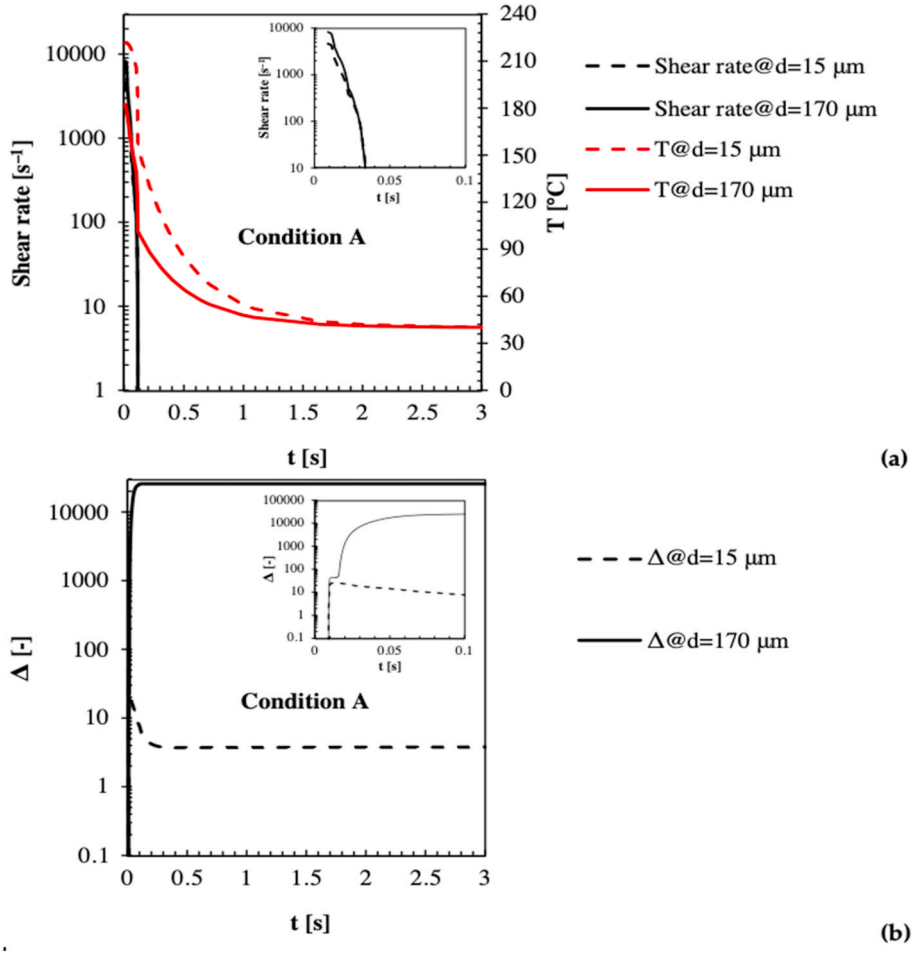

Fig. 4. Shear rate, temperature (a), and molecular stretch (b) evolutions at 6 mm downstream the cavity entrance for condition A. Two different distances from the midplane are considered: 15 μm and 170 μm.

becomes uniform and equal to the mold temperature within 2 s. The mold temperature is obviously achieved in advance for the layers at a larger distance from the midplane. Also, the values of the molecular stretch parameter, Δ, depend on the distance from the sample midplane. Close to the wall, the stretch increases and, within 0.1 s, reaches the final value (see inset in Fig. 4b). Toward the midplane, the stretch, after an initial increase, decreases and reaches a constant value within 0.2 s. The decrease of Δ, observed close to the sample midplane, is due to the high temperatures that promote the relaxation. As the material solidification proceeds, relaxation slows down and molecular stretch becomes constant after about 0.2 s. At larger distances from the sample midplane, the flow is more intense and the solidification is faster; thus, the relaxation process is less efficient in counteracting the effect of flow. At this distance from the midplane, Δ increases monotonically to a final value that

is higher with respect to the final stretch value at the midplane.

Fig. 5a and b shows shear rate, temperature, and molecular stretch evolutions calculated for condition C (mold temperature 140 °C) at the two distances from the sample midplane: 15 μm (close to the sample midplane), and 170 μm (it is the first distance from the sample core where fibrils formation is predicted by the crystallization model for condition C).

Close to the midplane, temperature decreases from the injection temperature to the mold value when polymer reaches the selected position (namely 6 mm from the cavity entrance). The cooling is faster close to the sample wall. After a fast cooling the temperature remains constant and essentially uniform along the thickness as long as the wall temperature is kept constant, i.e. before the mold is cooled down in the water bath. Δ evolution is similar to the one observed for condition A. With respect to condition A, close to the sample midplane, the final value of Δ is reached within longer times, this is due to a higher temperature field kept for long times, which determines both high relaxation degrees and smaller final values of Δ.

Fig. 6 shows, for all molding conditions (A, B and C), evolutions of temperature, fibril and spherulite crystallinity degrees ($\chi_f$and χ respectively) at 15 μm from the sample midplane.

In condition A, namely 40 °C mold temperature, only fibrils form during the process, whereas with higher mold temperatures essentially only spherulites form. The spherulites do not form even for longer times (i.e. 30 s) in condition A. At the lowest mold temperatures, the relaxation is less efficient in counteracting the flow effect on molecular stretch, which remains higher. Fibril crystallization kinetics are faster than the spherulitical ones, and the fibril structures completely fill the whole available volume. Essentially only fibrils form. Vice versa, with higher mold temperatures, namely in conditions B and C, essentially only spherulites form; this is due to the relaxation that efficiently counteracts the molecular stretch (due to the high temperature) and delays solidification. The lower value of Δ does not allow for fibril formation during the time that the mold remains at high temperatures. Material crystallization occurs only during the subsequent mold cooling: a quiescent non–isothermal spherulitic crystallization occurs and spherulites fill the whole available volume. As expected, spherulitic kinetics start within shorter times if a lower mold temperature is adopted.

Fig.7 shows, for all molding conditions, temperature and crystallinity degree evolutions at 90 μm (it is the first distance from the sample core where fibrils formation is predicted by the crystallization model for condition B).

Crystallinity evolutions in conditions A and C, shown in Fig. 7, are similar to the ones observed close to the sample midplane (Fig. 6). Condition B shows a different evolution of crystallinity: fibrils form within 1 s and completely fill the available volume, whereas close to the midplane, only spherulites are predicted (see Fig. 6). The shear rate increases from the midplane to the sample wall, consistently, the stretch also increases. In particular, at 90 μm from the sample midplane, the higher values of Δ, with respect to the midplane, give rise to a higher axial growth rate; thus, the fibrils formation can take place within 1 s from the process start.

Fig. 8 shows, for conditions B and C, the calculated final distributions along the sample half thickness of fibrillar and spherulitic crystallinity degrees. The optical micrographs of the sample half thickness are also shown for comparison. Fibrils completely fill the whole thickness in condition A.

Consistently with the experimental observations, the thickness of fibrillar layers decreases as mold temperature increases; conversely, thickness of spherulitical layers decreases as mold temperature

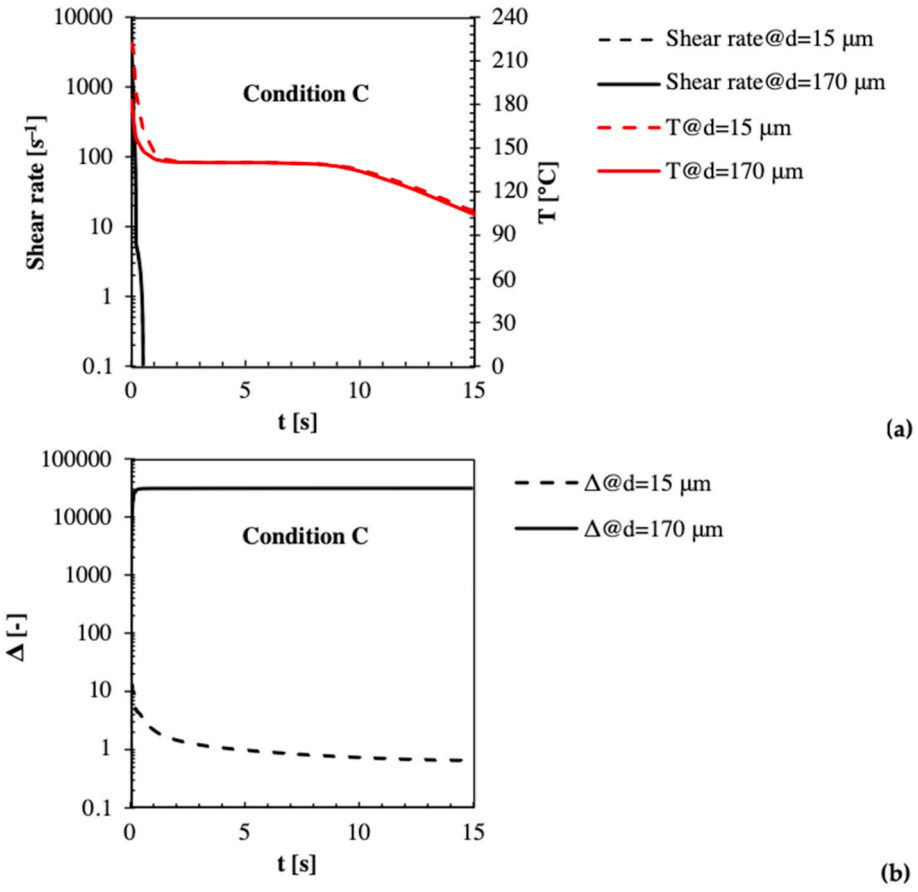

Fig. 5. Shear rate, temperature (a), and molecular stretch (b) evolutions at 6 mm downstream the cavity entrance for condition C (mold temperature 140 °C). Two different distances from the sample midplane are considered, 15 μm and 170 μm.

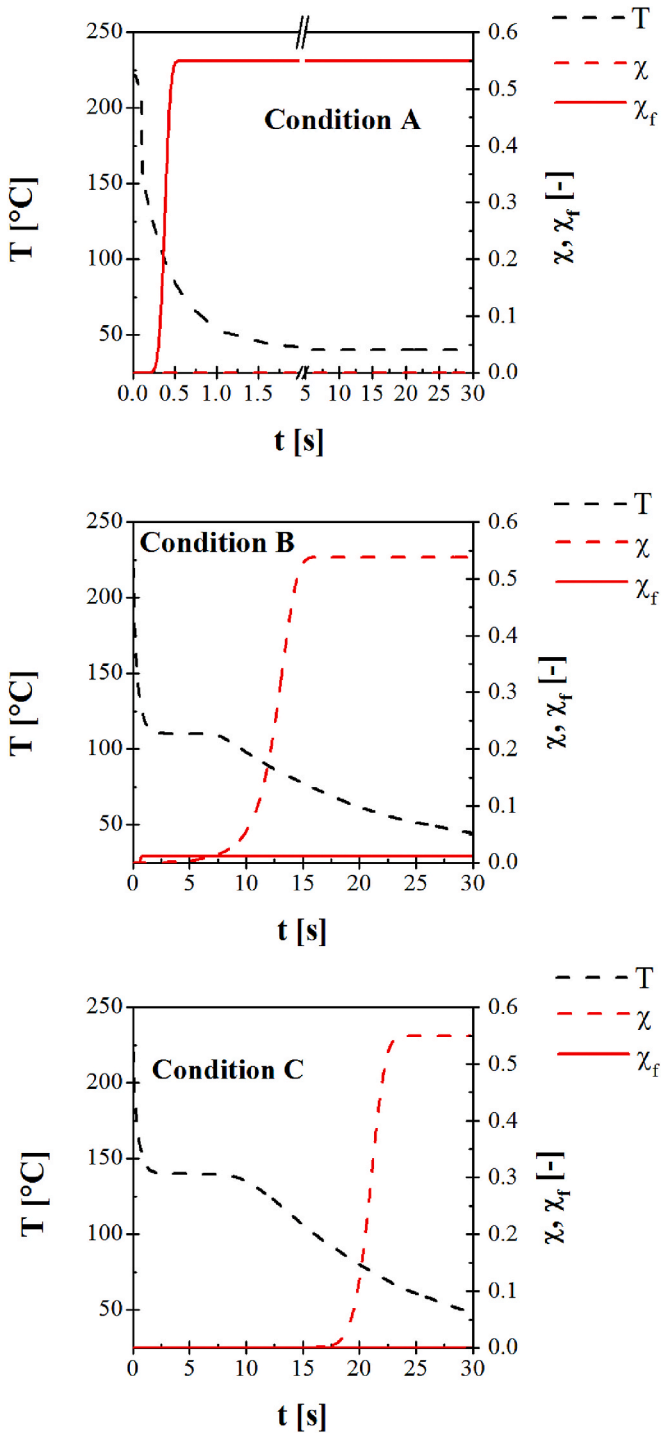

Fig. 6. Evolutions of temperature, spherulite and fibril crystallinity degrees at 15 μm from the sample midplane for all the molding conditions.

decreases, and spherulites do not form at all with 40 °C mold temperature.

With a mold temperature of 110 °C (condition B), as already described above, there is a transitional zone where both fibrils and spherulites are present. The predictions are consistent with this finding. Furthermore, the thicknesses of fibril and spherulitic layers are correctly predicted.

With a mold temperature of 140 °C (condition C), the predicted spherulitic layer thickness is larger than the experimental one. The prediction of the fibril layer extension for condition C would be more

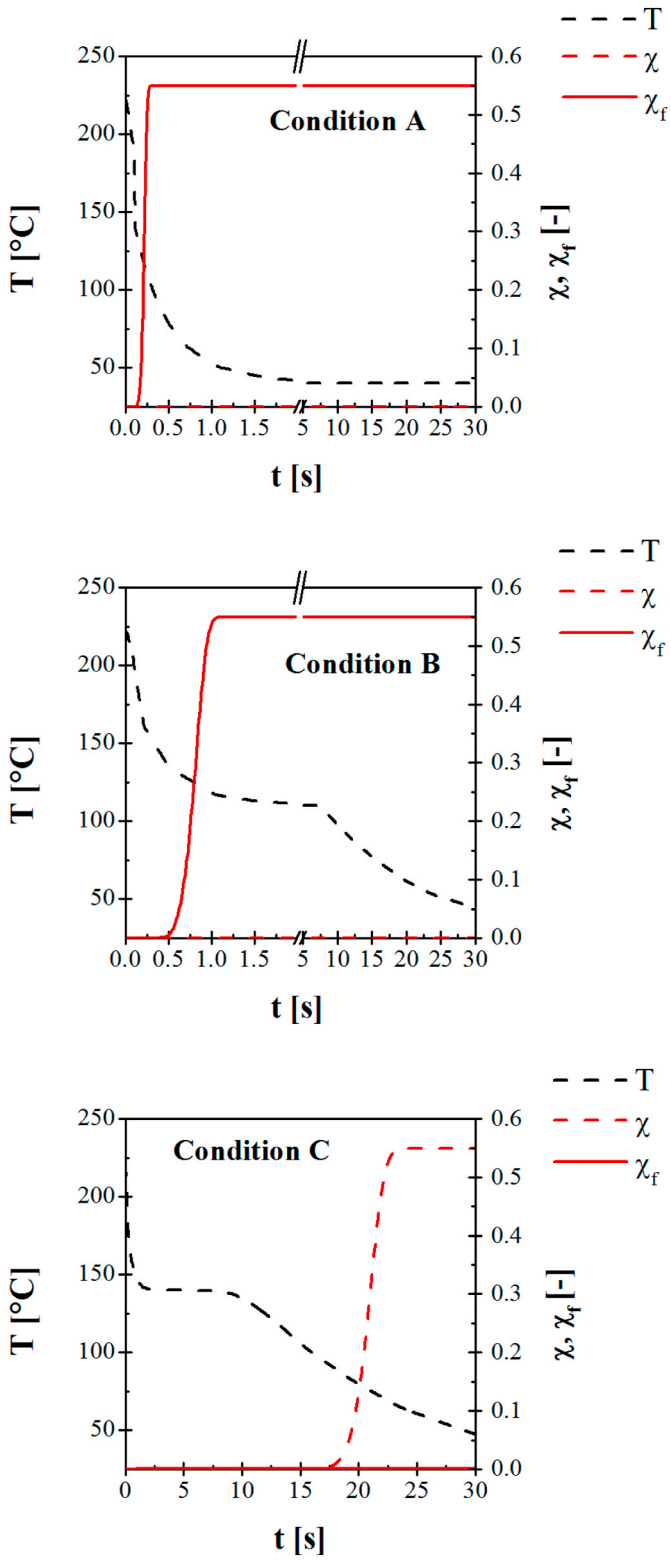

Fig. 7. Evolutions of temperature, spherulite and fibril crystallinity degrees at 90 μm from the sample midplane for all the molding conditions.

consistent with the experimental one if one would consider a smaller threshold value of Δ. It is worth mentioning that the fibril kinetics was tuned according to the results obtained at high temperature (the Linkam shearing tests were conducted at 140 °C and 150 °C), and it is assumed not to be directly dependent on temperature. Obviously, a temperature dependence on some parameter, for instance the threshold value of Δ

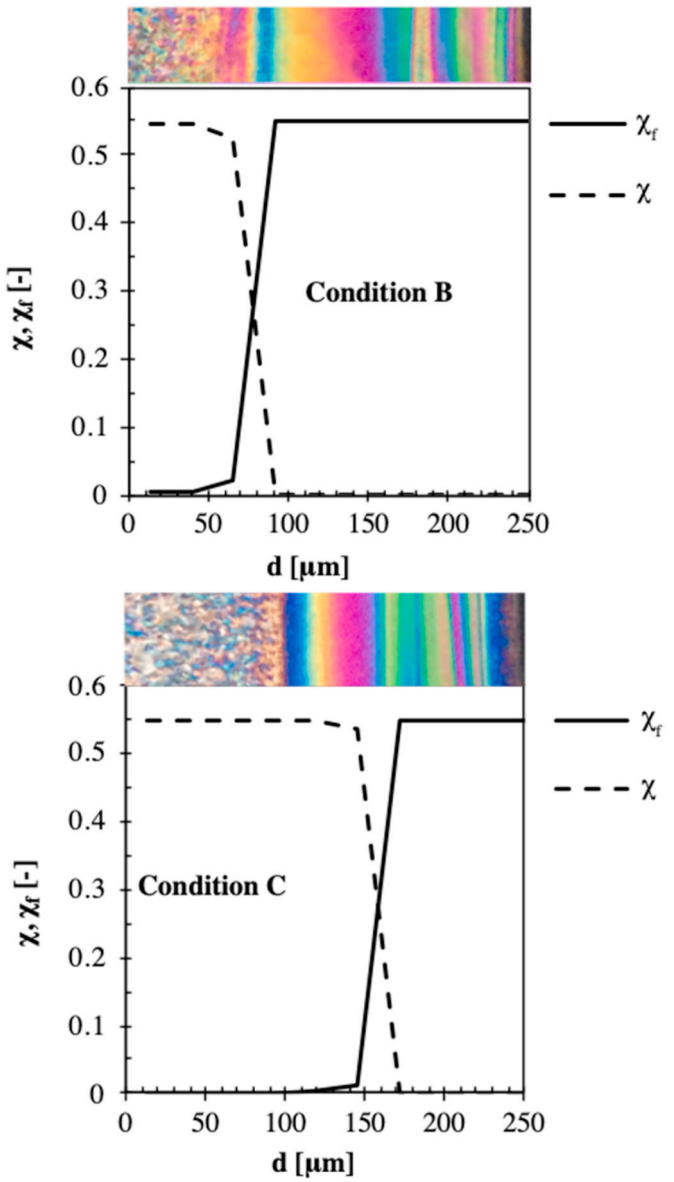

Fig. 8. Final distributions of spherulites and fibrils along the sample half thickness for molding conditions B and C.

would furtherly improve the comparison between simulation and experimental results.

For instance, it is possible to evaluate the extension of the fibrillar layer thickness assuming $\Delta_{min} = 2$ as threshold value for the molecular stretch. Fig. 9 shows the final distributions of spherulites and fibrils along the sample half thickness for molding condition C.

The prediction of the fibrillar layer thickness is more consistent with the experimental observation than the prediction obtained with $\Delta_{min} = 2.5$. However, the adoption of $\Delta_{min} = 2$ as critical molecular stretch value does not allow obtaining reliable results for the other considered molding conditions, A and B. This suggests that the critical molecular stretch value could vary with temperature.

Another aspect to be considered concerns the simulations conducted with Moldex3D. The model implemented in Moldex3D lacks of considering the interplay between the viscosity and the solidification, this is another reason for the discrepancy between the experimental data and simulations results of final flow length and fibrillar layer thickness.

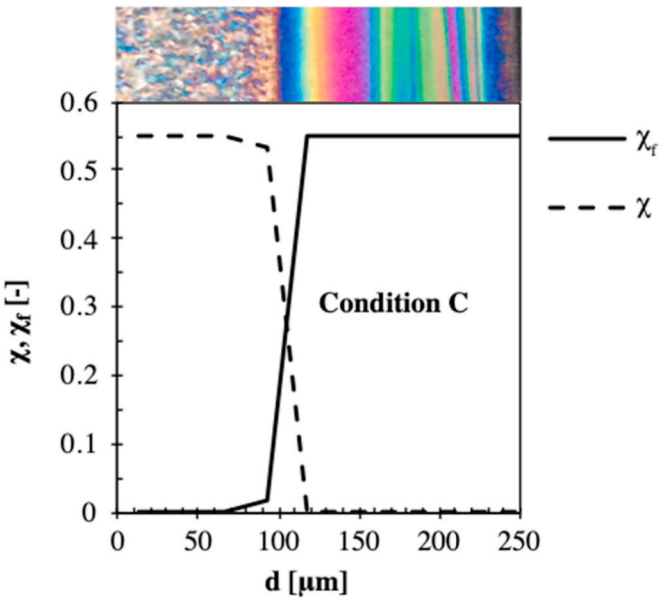

Fig. 9. Final distributions of spherulites and fibrils along the sample half thickness for molding conditions C, evaluated with $\Delta_{min} = 2$.

5. Conclusions

A model describing the formation of fibrils and spherulites was applied for describing the morphology evolutions during the micro–injection molding process. The crystallization model was coupled with the numerical simulations of the process, in particular with simulated shear rate and temperature evolutions, obtained adopting the commercial software Moldex3D. The temperature and flow field descriptions given by Moldex3D were compared with the final filling length experimentally observed during tests conducted with different mold temperatures. Moldex3D provided final filling length consistent with the experimental ones for high mold temperatures, whereas it predicted filling length longer than the experimental ones for low mold temperatures.

The updated crystallization model almost correctly predicted the thickness of the fibrillar layers for mold temperatures of 40 °C and 110 °C. In the former condition, the fibrillar kinetics overcame the spherulitical ones, and the fibrils occupied all the available volume. In the latter condition, the fibrillar kinetics overcame the spherulitical ones only in the layers closer to the sample walls, whereas, toward the core, the formation of spherulites was predicted. The crystallization model almost correctly predicted the decrease of the fibrillar layer thickness with the increase of the mold temperatures. In the condition with a mold temperature of 140 °C, the predicted fibrillar layer thickness was smaller than the experimental one. A more correct prediction of the fibrillar layer thickness would be achieved considering, at that temperature, a smaller threshold value of the molecular stretch, which, on its turns, would imply that the fibrillar kinetics depends on temperature.

The crystallinity significantly influences the material rheological behavior, thus, simulation software for the injection molding process should account also for the interplay between crystallization and material rheological properties. Considering this interplay would allow a better description of final filling length, also at low mold temperatures.

Declaration of competing interest

The authors declare that they have no known competing financial interests or personal relationships that could have appeared to influence the work reported in this paper.

Appendix A

In order to understand how the molecular orientation and stretch are related to the macroscopic flow field, mechanical models for the description of molecular arrangement are needed. The elastic dumbbell represents one of the simplest models for this purpose: a polymer molecule is represented by two beads connected by a non-bendable spring. The configuration of the dumbbell is given by the end-to-end vector **R**. Assuming that the molecules do not interact with one another and that the flow field can be considered homogeneous, the equation of change for the second-order conformation tensor **RR** in absence of external forces is given by equation (A1) [38].

$$\frac{D}{Dt}\langle \mathbf{RR}\rangle - (\nabla \boldsymbol{v})^T\cdot\langle \mathbf{RR}\rangle - \langle \mathbf{RR}\rangle\cdot(\nabla \boldsymbol{v}) = \frac{4kT}{\zeta}\boldsymbol{\delta} - \frac{4}{\zeta}\langle \mathbf{RF}\rangle \tag{A1}$$

where the symbol $\langle * \rangle$ is the average over the configuration space, $\nabla \boldsymbol{v}$ is the velocity gradient, k is Boltzmann constant, T is the temperature in K, ζ is the friction coefficient of the beads, $\boldsymbol{\delta}$ is the unity matrix and **F** is the force between the beads. The first term of LHS of equation (A1) is the substantial (material) derivative of $\langle \mathbf{RR}\rangle$ given by equation A2

$$\frac{D}{Dt}(*) = \frac{\partial}{\partial t}(*) + \boldsymbol{v}\cdot\nabla(*) \tag{A2}$$

The whole LHS is the codeformational derivative of $\langle \mathbf{RR}\rangle$. The first term of the RHS is due to the Brownian motion whereas the last term is due to the intramolecular force, namely, for the simple model adopted, the force acting on the beads through the spring. Assuming that the spring is Hookean, namely the tension between the beads is proportional to their separation and depends on the spring constant H, equation (A1) can be rewritten as

$$\frac{D}{Dt}\langle \mathbf{RR}\rangle - (\nabla \boldsymbol{v})^T\cdot\langle \mathbf{RR}\rangle - \langle \mathbf{RR}\rangle\cdot(\nabla \boldsymbol{v}) = \frac{4kT}{\zeta}\boldsymbol{\delta} - \frac{4H}{\zeta}\langle \mathbf{RR}\rangle \tag{A3}$$

In a system under quiescent condition at equilibrium, equation (A3) gives

$$\frac{4kT}{\zeta}\boldsymbol{\delta} = \frac{4H}{\zeta}\langle \mathbf{RR}\rangle_0 \tag{A4}$$

where $\langle \mathbf{RR}\rangle_0$ is the second order conformation tensor at rest in the equilibrium state. The end-to-end distance of the molecule is $\langle R_0^2\rangle$ (A5) and it can be obtained by considering the trace of equation (A4)

$$3\frac{4kT}{\zeta} = \frac{4H}{\zeta}\langle R_0^2\rangle \tag{A5}$$

Being the dumbbell relaxation time $\lambda = \zeta/4H$ and considering equation (A4), equation (A3) becomes

$$\frac{D}{Dt}\langle \mathbf{RR}\rangle - (\nabla \boldsymbol{v})^T\cdot\langle \mathbf{RR}\rangle - \langle \mathbf{RR}\rangle\cdot(\nabla \boldsymbol{v}) = \frac{1}{\lambda}\left[\langle \mathbf{RR}\rangle_0 - \langle \mathbf{RR}\rangle\right] \tag{A6}$$

Equation (A6) can be rewritten as [39].

$$\frac{D}{Dt}\boldsymbol{A} - (\nabla \boldsymbol{v})^T\cdot\boldsymbol{A} - \boldsymbol{A}\cdot(\nabla \boldsymbol{v}) + \frac{1}{\lambda}\boldsymbol{A} = (\nabla \boldsymbol{v}) + (\nabla \boldsymbol{v})^T \tag{A7}$$

with

$$\boldsymbol{A} = \frac{3}{R_0^2}\left[\langle \mathbf{RR}\rangle - \langle \mathbf{RR}\rangle_0\right] \tag{A8}$$

The second order tensor $\boldsymbol{A}$ (A8) is the fractional "deformation" of the chain with respect to its equilibrium conformation. Equation (A7) does not limit the deformation of the molecular chain. Combining equation A4 and A5, under quiescent condition, the equilibrium conformation tensor is given by equation (A9)

$$\langle \mathbf{RR}\rangle_0 = \frac{1}{3}\langle R_0^2\rangle\boldsymbol{\delta} \tag{A9}$$

Under quiescent condition when the beads coalesce $\langle \mathbf{RR}\rangle = 0$ and $\boldsymbol{A}$ reaches its minimum (A10), that is considering equations (A9) and (A8)

$$\boldsymbol{A} = \boldsymbol{\delta} \tag{A10}$$

It is worth to point out that equation (A7) allows describing the molecular stretch evolution during the process, once the velocity gradient, $\nabla \boldsymbol{v}$, and the relaxation time λ are known. In the classical elastic dumbbell model the relaxation time, λ, is constant and it is well known that with this choice the model is not able to predict the shear thinning behavior of polymer melts. However, in order to overcome this limitation, nonlinear dumbbell models are considered. Such a model adopts the same equation of change of the average molecular conformation [40], but assumes a non-constant relaxation time. In particular it was found that adopting a non-linear formulation of a dumbbell model with a relaxation time depending upon flow [41], in particular upon a molecular parameter [33] a reliable description of the molecular orientation evolution during the process can be achieved (A11).

$$\frac{D}{Dt}\boldsymbol{A} - (\nabla \boldsymbol{v})^T\cdot\boldsymbol{A} - \boldsymbol{A}\cdot(\nabla \boldsymbol{v}) + \frac{1}{\lambda(\boldsymbol{A})}\boldsymbol{A} = (\nabla \boldsymbol{v}) + (\nabla \boldsymbol{v})^T \tag{A11}$$

For simple shear flow, the velocity gradient is given by equation (A12)

$$(\nabla \boldsymbol{v}) = \begin{bmatrix} 0 & 0 & 0 \\ \dot{\gamma} & 0 & 0 \\ 0 & 0 & 0 \end{bmatrix} \tag{A12}$$

Thus, the evolution of $\boldsymbol{A}$ can be written as

$$\frac{D}{Dt}\begin{bmatrix} A_{11} & A_{12} & A_{13} \\ A_{21} & A_{22} & A_{23} \\ A_{31} & A_{32} & A_{33} \end{bmatrix} - \dot{\gamma}\begin{bmatrix} 2A_{12} & A_{22} & A_{23} \\ A_{22} & 0 & 0 \\ A_{23} & 0 & 0 \end{bmatrix} + \frac{1}{\lambda(\boldsymbol{A})}\begin{bmatrix} A_{11} & A_{12} & A_{13} \\ A_{21} & A_{22} & A_{23} \\ A_{31} & A_{32} & A_{33} \end{bmatrix} = \begin{bmatrix} 0 & \dot{\gamma} & 0 \\ \dot{\gamma} & 0 & 0 \\ 0 & 0 & 0 \end{bmatrix} \tag{A13}$$

where the subscript "1" identifies the flow direction, whereas the subscript "2" and "3" identify the transverse directions, namely sample thickness and width respectively. Assuming that for all the components of $\boldsymbol{A}$ both the initial and the boundaries' conditions are identically zero, namely $\langle \mathbf{RR} \rangle = \langle \mathbf{RR} \rangle_0$ when the flow starts and on the sample boundaries, equation (A13) becomes:

$$\frac{\partial A_{11}}{\partial t} - 2\dot{\gamma}A_{12} + \frac{A_{11}}{\lambda} = 0$$

$$\frac{\partial A_{12}}{\partial t} + \frac{A_{12}}{\lambda} - \dot{\gamma} = 0 \tag{A14}$$

It is worth mentioning that under isothermal conditions and in the presence of a homogeneous flow, convective terms disappear in equation (A14).

Appendix B

The original model for crystallization was validated by Linkam shearing tests conducted under controlled shear rates and isothermal conditions [26]. Times (grey symbols) at which the formation of the oriented structures was observed at each applied shear rate are shown in Fig. B1. The data are referred to tests conducted at 140 °C.

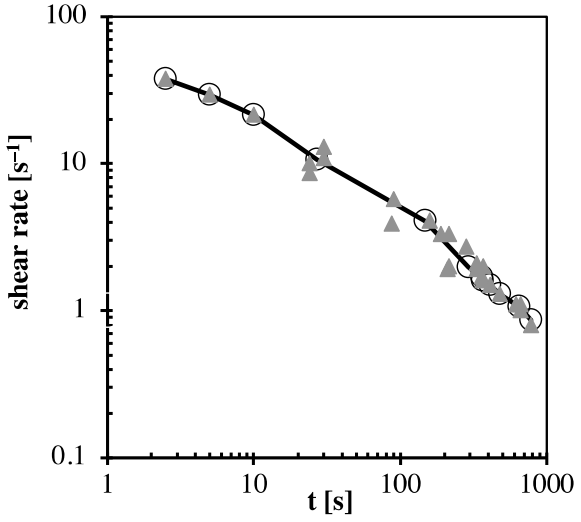

Fig. B1. Times required for fiber formations during Linkam shearing tests (grey symbols) conducted at 140 °C. Evaluations of those times are reported as black lines with markers.

It is worth to mentioning that for the shear tests conducted at temperature of 140 °C, applying shear rate higher than 40 s^{-1} the formation of fibers was not followed because the crystallization process was instantaneous, whereas with shear rate lower than 0.8 s^{-1} the formation of fibers was not observed, even for very long shearing times.

Firstly, shearing tests were analyzed with the model which assumed, as first attempt, that axial growth rate of fibrils was constant along the single shear test. Value of axial growth rate was identified in such a way to obtain the best possible description of the data reported in Fig. B1. The calculated times required for fiber formation are also shown in Fig. B1 as black lines with markers. Predictions are consistent with the experimental observations.

Figs B2a and B2b report the evolutions of the molecular stretch and of the overall crystallinity (determined by the amount of spherulites and fibers) respectively, calculated for a shearing test conducted with shear rate of 0.8 s^{-1} at 140 °C.Fig. B2a clearly shows that molecular stretch significatively changes during the test, even if under isothermal constant flow field. The molecular stretch, Δ, after an initial transient reaches its steady state value, which depends on the shear rate applied and on the value of the relaxation time. Δ remains constant as long as the overall crystallinity amount is of the order of a few percent. Due to the dependence of relaxation time on crystallinity (see equation (7)), as soon as the crystallinity reaches values of the order of 10%, the relaxation process becomes less effective in counteracting the effect of flow on the orientation and Δ starts to increase. On its turn, the increase of Δ enhances the crystallization kinetics, giving rise to a sharp increase of the molecular stretch. By effect of such a catastrophic process, crystallinity reaches its equilibrium value within a few tenths of seconds. As a result, for semi-crystalline materials, the solidification process induces a significant increase of the molecular stretch.

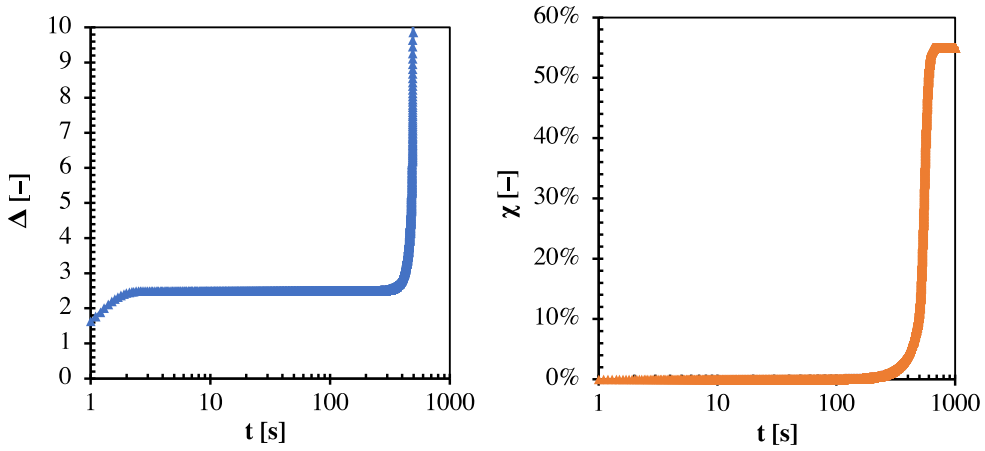

Fig. B2. Predicted evolution of **(a)** molecular stretch and (b) overall crystallinity during Linkam shearing test conducted at 140 °C with shear rate of 0.8 s^{-1}.

Fig. B3 shows the axial growth rates of fibrils (full symbols) and spherulites growth rates (open symbols) adopted to describe the crystallinity evolution during the Linkam shearing tests. Fig. B3 shows the values of G_f adopted in the model to obtain the prediction of the times required for fiber formations (see Fig. B1) plotted versus the Δsteady state value, namely the molecular stretch of the polymer in the molten state before the material crystallization.

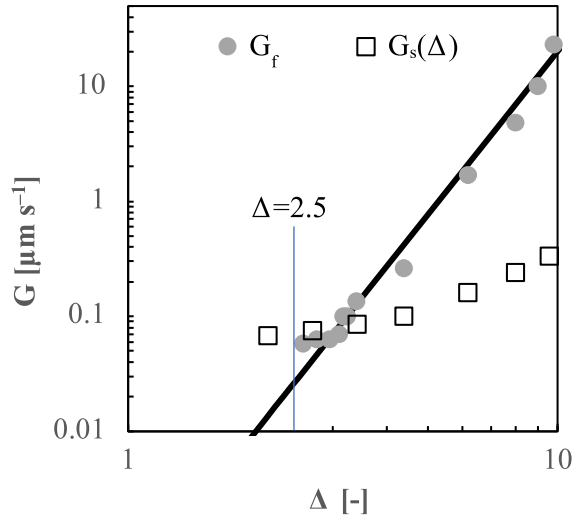

Fig. B3. The fibril axial growth rate and spherulite growth rate as function of the molecular stretch, Δ. The fibril lateral growth rate is also represented, being equal to the spherulite growth rate.

In a double log chart, the values of G_f follow a straight line. Therefore, the dependence of G_f upon the molecular stretch can be expressed as a power law and G_f can be described by equation (13). As the stretch level increases, the fibril formation becomes faster and overcomes the spherulite formation. In order to obtain fibrils, the axial growth rate has to be significantly higher than the lateral one. Furthermore, fibrils neither form nor grow when low molecular stretches, namely shear rates, are attained as shown by Linkam shearing tests. Therefore, a threshold value of the molecular stretch, $\Delta_{min} = 2.5$, was introduced, which corresponds to the lowest shear rate at which fibrils can be observed, namely 0.8 s^{-1}.

Fig. B4 , referred to the Linkam shearing tests, shows the comparison between the final fibril amounts, obtained adopting the model given in Ref. [26] and the one evaluated adopting the model proposed in this work. In the first model, fibrils form for any Δ, whereas in the model developed in this work, a threshold value for fibrils formation, Δ_{min} equal to 2.5, was assumed. For values of shear rates higher than 0.8 s^{-1}, the two models predict almost the same percentage of fibrils, i.e. higher than 30% of fibrils. For values of shear rates lower than 0.8 s^{-1}, the amount of fibrils predicted adopting the updated model is significantly smaller than that predicted adopting the model given in Ref. [26].

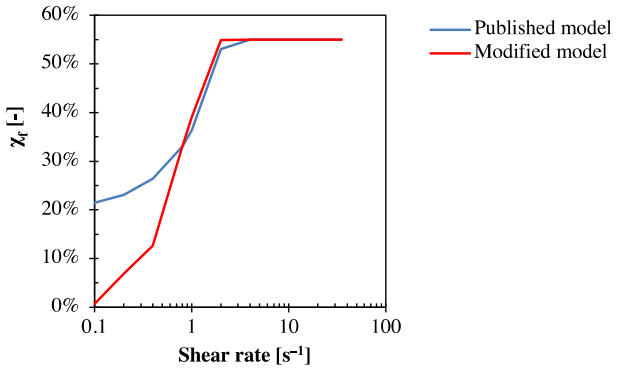

Fig. B4. Predictions of final fibril amounts for different shear rate calculated with published model and model adopted in present work.

In particular, adopting the updated model the formation of fibers is prevented for shear rate lower than 0.1 s^{-1}. Furthermore, for shear rate ranging from 0.2 to 0.7 s^{-1} the introduction of the threshold mechanism efficiently reduces the final content of fibers. This is more consistent with the experimental tests in which the absence of fibrils was observed at shear rates lower than 0.7 s^{-1}. This can be ascribed to the evolution of Δ during the shearing test. Fig. B5 shows the evolution of spherulitic and fibril crystallinity during shearing test with imposed shear rate of 0.7 s^{-1}. During that test, the initial plateau value of Δ (namely before crystallization start) is below the threshold value and only spherulites can form. As the overall crystallinity reaches value of order of 10%, the orientation induced by the flow is not efficiently counteracted by the relaxation process (due to the increase of relaxation time essentially by effect of the spherulitic crystallinity). Thus, the molecular orientation increases and the fibrillar crystallization starts as soon as Δ overcomes the threshold value. Fibrillar crystallization proceeds faster than the spherulitic one and the available space is rapidly filled by fibers (about 30%) with a significant fraction of spherulites.

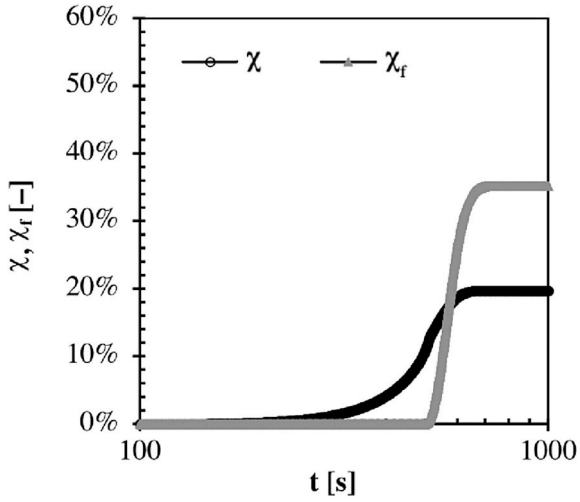

Fig. B5. Predicted evolution of spherulitic and fibrillar crystallinity during Linkam shearing test conducted at 140 °C with shear rate of 0.7 s^{-1}.

Appendix C. Supplementary data

Supplementary data related to this article can be found at https://doi.org/10.1016/j.polymer.2021.123850.

References

[1] Q. Su, N. Zhang, M.D. Gilchrist, The use of variotherm systems for microinjection molding, J. Appl. Polym. Sci. 133 (2016) (n/a-n/a).
[2] A. Ameli, Y. Kazemi, S. Wang, C.B. Park, P. Pötschke, Process-microstructure-electrical conductivity relationships in injection-molded polypropylene/carbon nanotube nanocomposite foams, Composer Part A Appl. Sci. Manuf. 96 (2017) 28–36.
[3] G. Eder, H. Janeschitz-Kriegl, P.-C. Chang, S.-J.Y. Hwang, C. Weng, W.B.Y.D. Lee, S. To, V. Piotter, T. Hanemann, R. Ruprecht, et al., Injection molding handbook, Polymer 42 (2009) 1–5.
[4] D. Mi, C. Xia, M. Jin, F. Wang, K. Shen, J. Zhang, Quantification of the effect of shish-kebab structure on the mechanical properties of polypropylene samples by controlling shear layer thickness, Macromolecules 49 (2016) 4571–4578.
[5] Z. Zhao, Q. Yang, M. Kong, D. Tang, Q. Chen, Y. Liu, F. Lou, Y. Huang, X. Liao, Unusual hierarchical structures of micro-injection molded isotactic polypropylene in presence of an in situ microfibrillar network and a β-nucleating agent, RSC Adv. 5 (2015) 43571–43580.
[6] G. Kalay, M.J. Bevis, Injection Molding of Isotactic Polypropylene, 1999, pp. 329–334.
[7] J. Jiang, S. Wang, B. Sun, S. Ma, J. Zhang, Q. Li, G.-H. Hu, Effect of mold temperature on the structures and mechanical properties of micro-injection molded polypropylene, Mater. Des. 88 (2015) 245–251.
[8] J. Jiang, X. Liu, M. Lian, Y. Pan, Q. Chen, H. Liu, G. Zheng, Z. Guo, D.W. Schubert, C. Shen, et al., Self-reinforcing and toughening isotactic polypropylene via melt sequential injection molding, Polym. Test. 67 (2018) 183–189.
[9] X. Wang, Y. Pan, Y. Qin, M. Voigt, X. Liu, G. Zheng, Q. Chen, D.W. Schubert, C. Liu, C. Shen, Creep and recovery behavior of injection-molded isotactic polypropylene with controllable skin-core structure, Polym. Test. 69 (2018) 478–484.
[10] M. Zhou, X. Li, M. Jin, C. Xia, K. Shen, J. Zhang, Simultaneously improving the tensile and impact properties of isotactic polypropylene with the cooperation of co-PP and β-nucleating agent through pressure vibration injection molding, Chin. J. Polym. Sci. 34 (2016) 1001–1013.

[11] M. Kuzmanović, L. Delva, L. Cardon, K. Ragaert, The effect of injection molding temperature on the morphology and mechanical properties of PP/PET blends and microfibrillar composites, Polymers 8 (2016) 355.
[12] P. Zhao, W. Yang, X. Wang, J. Li, B. Yan, J. Fu, A novel method for predicting degrees of crystallinity in injection molding during packing stage, Proc. Inst. Mech. Eng. Part B J. Eng. Manuf. 233 (2019) 204–214.
[13] G. Laschet, H. Nokhostin, S. Koch, M. Meunier, C. Hopmann, Prediction of effective elastic properties of a polypropylene component by an enhanced multiscale simulation of the injection molding process, Mech. Mater. 140 (2020), 103225.
[14] J. Guo, K.A. Narh, Computer simulation of stress-induced crystallization in injection molded thermoplastics, Polym. Eng. Sci. 41 (2001) 1996–2012.
[15] E. Koscher, R. Fulchiron, Influence of shear on polypropylene crystallization: morphology development and kinetics, Polymer 43 (2002) 6931–6942.
[16] D.J. Read, C. McIlroy, C. Das, O.G. Harlen, R.S. Graham, PolySTRAND model of flow-induced nucleation in polymers, Phys. Rev. Lett. 124 (2020), 147802.
[17] O.O. Mykhaylyk, P. Chambon, R.S. Graham, J.P.A. Fairclough, P.D. Olmsted, A. J. Ryan, The specific work of flow as a criterion for orientation in polymer crystallization, Macromolecules 41 (2008) 1901–1904.
[18] O.O. Mykhaylyk, P. Chambon, C. Impradice, J.P.A. Fairclough, N.J. Terrill, A. J. Ryan, Control of structural morphology in shear-induced crystallization of polymers, Macromolecules 43 (2010) 2389–2405.
[19] H. Janeschitz-Kriegl, E. Ratajski, M. Stadlbauer, Flow as an effective promotor of nucleation in polymer melts: a quantitative evaluation, Rheol. Acta 42 (2003) 355–364.
[20] P. Van Puyvelde, F. Langouche, J. Baert, Flow-induced crystallization in poly-1-butene: the shish-kebab transition, Int. J. Material Form. 1 (2008) 667–670.
[21] R. Pantani, V. Speranza, G. Titomanlio, A criterion for the formation of fibrillar layers in injection molded parts, Int. Polym. Process. 33 (2018) 355–362.
[22] S. Liparoti, V. Speranza, R. Pantani, G. Titomanlio, Process induced morphology development of isotactic polypropylene on the basis of molecular stretch and mechanical work evolutions, Materials 12 (2019).
[23] X. Wang, J. Ouyang, W. Zhou, Z. Liu, A phase field technique for modeling and predicting flow induced crystallization morphology of semi-crystalline polymers, Polymers 8 (2016) 230.
[24] G. Grosso, E.M. Troisi, N.O. Jaensson, G.W.M. Peters, P.D. Anderson, Modelling flow induced crystallization of IPP: multiple crystal phases and morphologies, Polymer 182 (2019), 121806.
[25] P.C. Roozemond, T.B. van Erp, G.W.M. Peters, Flow-induced crystallization of isotactic polypropylene: modeling formation of multiple crystal phases and morphologies, Polymer 89 (2016) 69–80.
[26] V. Speranza, S. Liparoti, V. Volpe, G. Titomanlio, R. Pantani, Modelling of morphology development towards spherulites and shish–kebabs: application to isothermal flow-induced crystallization experiments on isotactic polypropylene, Polymer 196 (2020), 122459.
[27] S. Liparoti, V. Speranza, A. Sorrentino, G. Titomanlio, Mechanical properties distribution within polypropylene injection molded samples: effect of mold temperature under uneven thermal conditions, Polymers 9 (2017) 585.
[28] S. Liparoti, A. Sorrentino, G. Guzman, M. Cakmak, G. Titomanlio, Fast mold surface temperature evolution: relevance of asymmetric surface heating for morphology of iPP molded samples, RSC Adv. 5 (2015) 36434–36448.
[29] R. Pantani, V. Speranza, G. Titomanlio, Effect of flow-induced crystallization on the distribution of spherulite dimensions along cross section of injection molded parts, Eur. Polym. J. 97 (2017) 220–229.
[30] R. Pantani, V. Speranza, G. Titomanlio, Thirty years of modeling of injection molding. A brief review of the contribution of unisa code to the field, Int. Polym. Process. 31 (2016) 655–663.
[31] S. Liparoti, V. Speranza, G. Titomanlio, R. Pantani, Effect of rapid mold heating on the structure and performance of injection-molded polypropylene, Polymers 12 (2020) 341.
[32] R. Pantani, F. De Santis, V. Speranza, G. Titomanlio, Analysis of flow induced crystallization through molecular stretch, Polymer 105 (2016) 187–194.
[33] R. Pantani, V. Speranza, G. Titomanlio, Orientation distribution in injection molding: a further step toward more accurate simulations, Rheol. Acta 51 (2012) 1041–1050.
[34] R. Pantani, V. Speranza, G. Titomanlio, Simultaneous morphological and rheological measurements on polypropylene: effect of crystallinity on viscoelastic parameters, J. Rheol. 59 (2015) 377–390.
[35] R. Pantani, V. Nappo, F. De Santis, G. Titomanlio, Fibrillar morphology in shear-induced crystallization of polypropylene, Macromol. Mater. Eng. 299 (2014) 1465–1473.
[36] S. Liparoti, V. Speranza, A. De Meo, F. De Santis, R. Pantani, Prediction of the maximum flow length of a thin injection molded part, J. Polym. Eng. (2020) 40.
[37] V. Speranza, S. Liparoti, R. Pantani, G. Titomanlio, Hierarchical structure of iPP during injection molding process with fast mold temperature evolution, Materials 12 (2019).
[38] Byron Bird, R.; Curtiss, C.F.; Armstrong, R.C.; Hassager, O. Dynamics of Polymeric Liquids: Kinetic Theory: 2. In; John Wiley and Sons, N.Y., Ed.; Wiley-Interscience, 1987; p. 63 ISBN 978-0-471-80244-0.
[39] V. Speranza, Analysis Ans Simulation of the Injection Molding Process. Prediction of the Morphology in Injection Molded Object, University of Salerno, 1999.
[40] G. Marrucci, Dynamics of entanglements: a nonlinear model consistent with the Cox-Merz rule, J. Nonnewton. Fluid Mech. 62 (1996) 279–289.
[41] R. Pantani, V. Speranza, A. Sorrentino, G. Titomanlio, Molecular orientation and strain in injection moulding of thermoplastics, Macromol. Symp. 185 (2002) 293–307.